



Mineral inclusions are not immutable: Evidence of post-entrapment thermally-induced shape change of quartz in garnet

Bernardo Cesare^{a,*}, Matteo Parisatto^a, Lucia Mancini^{b,c}, Luca Peruzzo^d, Marco Franceschi^e, Tommaso Tacchetto^f, Steven Reddy^f, Richard Spiess^a, Fabrizio Nestola^a, Federica Marone^g

^a Department of Geosciences, University of Padova, via G. Gradenigo 6, 35131 Padova, Italy

^b Elettra - Sincrotrone Trieste S.C.p.A., S.S. 14 - km 163.5 in AREA Science Park, 34149 Basovizza, Italy

^c LINXS - Lund Institute for Advanced Neutron and X-ray Science, Lund, Sweden

^d Istituto di Geoscienze e Georisorse, CNR, via G. Gradenigo 6, 35131 Padova, Italy

^e Department of Mathematics and Geosciences, University of Trieste, via E. Weiss, 2, 34128 Trieste, Italy

^f School of Earth and Planetary Sciences, Curtin University, Bentley 6102, Perth, Australia

^g Paul Scherrer Institut, Photon Science Department, WBB/216, Forschungsstrasse 111, CH-5232 Villigen, Switzerland

ARTICLE INFO

Article history:

Received 19 September 2020

Received in revised form 23 November 2020

Accepted 5 December 2020

Available online xxxx

Editor: R. Dasgupta

Keywords:

petrology

inclusions

quartz

garnet

X-ray tomographic microscopy

ABSTRACT

Sheltered inside crystals, mineral inclusions preserve crucial information on the geological history of our planet. These inclusions allow estimation of the pressure and temperature trajectories of metamorphic rocks, but also can tell about rock mineralogy, provenance, and geodynamic and petrogenetic processes. This information is recovered under the axiom that mineral inclusions have remained immutable objects that do not change shape after their entrapment. Conversely, we show that post-entrapment shape modifications do occur in high-T rocks from granulite-facies conditions.

Here we analyze the shape and orientation of quartz inclusions within garnet, a common metamorphic mineral. Our data reveal a progressive change in shape from irregularly-shaped forms in rocks formed at $T < 550^\circ\text{C}$, to combined dodecahedron and icositetrahedron geometries imposed by the host garnet in granulites equilibrated at $T > 750^\circ\text{C}$. Lack of fluid at the quartz-garnet phase boundary indicates that inclusion shape change occurs by thermally-induced grain boundary diffusion, driven by the minimization of the surface energy of the host-inclusion system.

Since inclusions acquire a negative crystal shape after entrapment, our discovery redefines the conceptual framework for the application of elastic thermobarometry, and motivates a reevaluation of the criteria for mineral inclusion syngensis in metamorphic rocks.

© 2020 Elsevier B.V. All rights reserved.

1. Introduction

Inclusions of fluids, melts, or minerals trapped within larger mineral grains are armoured from geological events that may affect the host rock after entrapment. Therefore, the investigation of such inclusions often represents the only way to investigate processes, whose traces would be otherwise lost, that occur in our planet (Roedder, 1984; Hopkins et al., 2008; Liu et al., 2017; Ferrero and Angel, 2018) and other planetary bodies (Blamey et al., 2015; Nabiei et al., 2018).

In metamorphic rocks, mineral inclusions constrain the tempo and mode of geodynamic processes in that they can be used to

infer temperature (T) (Zack et al., 2004), pressure (P) (Chopin, 1984), chemical composition of rocks and magmas (Walter et al., 2011), and environmental conditions (Wilde et al., 2001) in the lithosphere and lower mantle (Nestola et al., 2018) over time (Rubatto et al., 2011).

Traditional methods of determining P and T during metamorphism (St-Onge, 1987) from inclusions have recently been augmented by elastic geothermobarometry (Kohn, 2014; Angel et al., 2014): a technique that is mostly applied to quartz inclusions in garnet (Spear et al., 2014) as this inclusion-host pair is ubiquitous and easy to analyze by micro-Raman spectroscopy (Kohn, 2014; Bonazzi et al., 2019). A fundamental assumption in this approach is that the quartz included in garnet undergoes elastic dilational changes in volume in response to changes in P and T , but that irreversible strain is negligible and inclusion shape remains unchanged. This principle of immutable inclusion shape is general

* Corresponding author.

E-mail address: bernardo.cesare@unipd.it (B. Cesare).

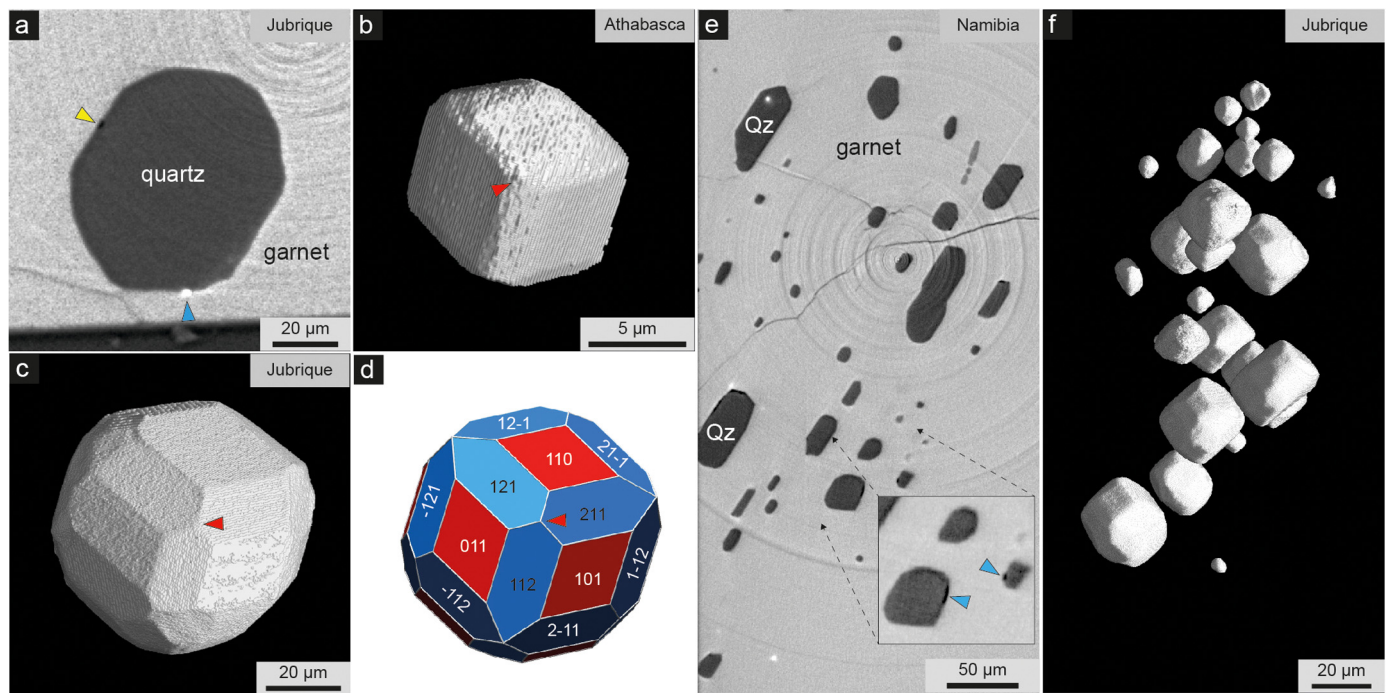


Fig. 1. Faceted, negative crystal quartz inclusions in granulite-facies garnet. **a**, SRXTM axial slice showing abundant straight (i.e., planar) garnet/quartz interfaces. Arrows point to a heavy inclusion (blue) and to a possibly fluid-filled pore (yellow) located at the interphase boundary. **b**, 3D rendering of the FIB-SEM serial sectioning of a quartz inclusion, showing well-developed facets arranged according to a morphological cubic symmetry. The red arrow points to the emergence of a 3-fold axis. **c**, 3D rendering of a faceted quartz inclusion reconstructed from SRXTM data. The facets of a dodecahedron and an icositetrahedron are superbly combined. Red arrow as in **b**. **d**, model of cubic crystal with morphology given by combination of dodecahedron {110} and icositetrahedron {211}, showing perfect analogy with the quartz inclusion reconstructed in **c**. Red arrow as in **b**. The model was generated with KrystalShaper v. 1.5.0 software by Steffen Weber (© JCrystalSoft, 2018, <http://www.jcrystal.com/products/krystalshaper/>). **e**, SRXTM 2D axial slice intersecting a cluster of quartz inclusions in garnet. Inclusions are faceted and show common orientation of facets. Inset enlarges a region with black areas at the quartz-garnet interface (blue arrows) which are interpreted as fluid-filled pores. **f**, 3D rendering from SRXTM data of a cluster of very small quartz inclusions showing marked polyhedral shape and sharing orientation of facets. Sample provenance is reported on the upper right corner of each panel.

to most studies of other inclusion-host pairs. For example, it represents a microstructural axiom for interpreting the origin of inclusions in diamonds (Harris, 1968) and constraining the timing of diamond formation (Richardson et al., 1984). Obviously, the possibility of a change of shape of inclusions within their host would greatly impact on the applications of elastic barometry, as well as on all other approaches that require or assume inclusions to maintain a constant shape.

A few rare studies have suggested that the shape of mineral inclusions evolves after trapping so as to minimize the interfacial free energy of the host-inclusion system (Vernon, 2004), and propose that this process leads to rounded shapes (Toriumi, 1979; Vernon, 1999; Okamoto and Michibayashi, 2005), a sphere being the solid with the lowest surface/volume ratio. In contrast, in fluid and melt inclusions (Roedder, 1984; Bodnar et al., 1985; Gualda et al., 2012), diffusion-controlled *shape maturation* is well known and manifests itself in inclusions as *negative crystal* shapes, i.e., the inclusions become polyhedral with their facets corresponding to rational planes of the host crystal (Fig. 1).

Here we test the possibility of shape change of solid inclusions following their entrapment by the application of 3D microstructural and crystallographic characterization of carefully selected samples. Inclusions of quartz in garnet were characterized using a high (sub-micrometric) spatial resolution workflow that included optical and scanning electron (SEM) microscopy, electron backscatter diffraction (EBSD), synchrotron radiation X-ray tomographic microscopy (SRXTM), micro-Raman spectroscopy, focused ion beam (FIB) serial slicing in the SEM and single-crystal X-ray diffraction (XRD). First, we demonstrate that in granulite-facies samples from high- T ($>750^\circ\text{C}$) rocks, quartz inclusions in garnet are not rounded nor irregular, but systematically show a polyhedral shape controlled by the surrounding host. Second, by compar-

ing these shapes and textures with those from greenschist-facies low- T ($<550^\circ\text{C}$) rocks, we address the general process of shape maturation for quartz inclusions in garnet. Finally, we argue that these processes are relevant to other mineral inclusion-host pairs, as well as to microstructure development in ceramics.

2. Materials and methods

2.1. Samples

The investigated samples are metasedimentary rocks of different grade: five (named Athabasca, Jubrique, Massachusetts, Namibia, and Swaziland) are high- or ultra-high- T granulite-facies metapelites metamorphosed at T in the range $750\text{--}1000^\circ\text{C}$; two (named eastern Alps and Tauern) are low-grade schist metamorphosed at $T < 550^\circ\text{C}$ and displaying typical greenschist-facies assemblages.

Sample Athabasca, from the Upper Deck domain of the Athabasca granulite terrane (Canada), is the fine-grained paragneiss sample 05G-019B of Dumond et al. (2015) containing garnet, ternary feldspar, quartz, kyanite, sillimanite, with minor plagioclase and biotite. This rock, in which sillimanite appears to predate kyanite, reached 1000°C at 1.6 GPa along a counterclockwise path (Dumond et al., 2015). Quartz inclusions occur with nanogranitoids at the core of the small $\text{Alm}_{61\text{--}64}\text{Prp}_{30\text{--}33}\text{Sps}_1\text{Grs}_{4\text{--}9}$ garnets (Tacchetto et al., 2019), which formed at about 800°C and 0.8 GPa.

Sample Jubrique, is a polymetamorphic granulitic gneiss of the Jubrique unit (Betic Cordillera, S Spain). The mineral assemblage in this rock with a high- T mylonitic fabric is garnet, quartz, plagioclase, K-feldspar, kyanite, sillimanite and cordierite, with rare biotite. Textural evidence indicates that sillimanite postdates kyanite. This sample reached a T of $\approx 850^\circ\text{C}$ and a pressure of 1.2–1.4 GPa

along a clockwise path characterized by almost isothermal decompression to 0.5–0.6 GPa (Barich et al., 2014). Quartz inclusions occur with nanogranitoids throughout the Alm₆₅Prp₂₈Sps₂Grs₅ garnets, which may reach 20 mm in diameter.

Sample Massachusetts, from Sturbridge in the Merrimack synclinorium (central Massachusetts, USA), is the cordierite-rich garnet granulite Sturb 1 studied by Thomson (2001). It contains garnet, cordierite, sillimanite, quartz, plagioclase, biotite and minor K-feldspar, and equilibrated at about 750 °C and 0.5 GPa along an inferred counterclockwise *P-T-t* path. The garnet has composition Alm₇₀Prp₂₅Sps₂Grs₃.

Sample Namibia is a fine-grained, garnet-rich paragneiss collected near Aus, and belongs to the Garub sequence of the Aus granulite terrain (Namibia). The foliated sample contains cordierite–sillimanite–garnet–biotite-rich layers and garnet–K-feldspar–quartz-rich layers. Metamorphism in these rocks reached peak conditions of 825 °C at 0.55 GPa (Diener et al., 2013). The small garnets are rich in quartz inclusions at their core, without nanogranitoids, and have composition Alm_{83–85}Prp_{10–13}Sps_{2–3}Grs₂.

Sample Swaziland, from the Mkhondo Valley Metamorphic Suite, Swaziland, is the fine-grained metapelitic migmatite Mk2 of Taylor et al. (2010). The Al₂SiO₅-free assemblage of the rock is garnet, cordierite, biotite, quartz, plagioclase, minor K-feldspar, and equilibrated at peak metamorphic conditions of 830–850 °C and 0.4 GPa. This sample contains abundant 1–2 mm garnet poikiloblasts (composition Alm_{74–81}Prp_{24–16}Sps₁Grs₂) characterized by numerous, lobate 10–300 µm quartz inclusions.

Sample eastern Alps is a chlorite-muscovite-garnet schist from an unknown locality in the eastern Alps, available in the teaching collection of the Department of Geosciences of the University of Padova (Italy). It contains garnet porphyroblasts <3 mm in diameter, rich in quartz inclusions, and formed at lower greenschist-facies conditions (*T* < 450 °C). Their composition is Alm_{65–74}Prp_{3–7}Sps_{13–2}Grs_{19–17} (Cesare et al., 2019).

Sample Tauern is a biotite-chlorite-garnet-muscovite graphitic schist collected on the Italian side of the Pfitscher Joch in the SW Tauern Window. The Alpine metamorphism in the area did not exceed 520 ± 30 °C and 0.65 ± 0.1 GPa (Selverstone and Munoz, 1987). Abundant, Alm_{62–75}Prp_{6–11}Sps_{10–2}Grs_{23–12} euhedral garnets up to 4 mm in diameter are filled with quartz inclusions defining an internal foliation.

2.2. Synchrotron Radiation X-ray Tomographic Microscopy (SRXTM) experiments

Discs of garnet containing quartz inclusions were microdrilled from doubly-polished thick sections of all the samples. Targets for microdrilling were selected by careful optical petrography, and each disc contains a fragment of a single garnet crystal. The diameter of the discs ranges from 0.5 to 1 mm and the thickness from 0.2 to 0.3 mm approximately. Each sample was then glued with cyanoacrylate onto the tip of a glass capillary that was fixed on a cylindrical brass holder. 36 garnet fragments were analyzed.

SRXTM experiments were carried out at the TOMCAT beamline (Stampanoni et al., 2006) of the Swiss Light Source (SLS) at the Paul Scherrer Institut (Villigen, Switzerland). A beam energy of 25 keV and a sample-to-detector distance of 7 mm were selected as an optimal configuration for the investigated samples, operating in propagation-based phase-contrast mode (Baruchel et al., 2000) to obtain edge-enhancement effects. For each tomographic scan, 1800 X-ray radiographs were acquired with an angular step of 0.1° over a 180° rotation by a detection system constituted of: a) a LuAG:Ce scintillator (CRYTUR spol. s.r.o., Czech Republic) with a thickness of 20 µm; b) a 20x magnification optical microscope (Optique Peter, France); c) a low noise and large field of view *pcO. Edge 5.5*

CMOS camera (PCO AG, Germany) with 16-bit dynamic range, 2560 x 2160 pixels and 6.5 µm physical pixel size.

Reconstructions of axial slices (isotropic voxel size of 325 nm), including single-distance phase-retrieval post-processing of X-ray radiographs (Paganin et al., 2002), were carried out using the Gridrec fast reconstruction algorithm (Marone and Stampanoni, 2012) in use at the TOMCAT beamline. The real spatial resolution can be roughly assumed as 2–3 times the actual voxel size. Although samples often exceeded the detector field of view at some rotation angles and in spite of the relatively high absorption of the garnets, the selected experimental parameters allowed obtaining high quality tomographic images, showing good contrast between different phases, with very limited artefacts.

2.3. Analysis of SRXTM data

The analysis of tomographic data started from a qualitative evaluation of the acquired datasets (both on reconstructed slices and volumes) and a selection of the most significant samples in terms of amount, size and shape of inclusions. The attention was focused in particular on polyhedral quartz and biotite inclusions, ranging in size from 25–30 µm to 90–100 µm. Inclusions were segmented from their host garnet and other phases (e.g. small voids and high-density minerals at the host/inclusion interface) by means of a customized image processing protocol based on grey level thresholding, despeckling and morphological operations. In particular, 3D opening (erosion followed by dilation) was used to remove small surface irregularities caused by a non-perfect greyscale thresholding of the inclusions. The procedure also permitted the removal, or a significant reduction, of most image artifacts and other undesired features (e.g. cracks), with the aim of highlighting the facets of the inclusions with minimal alteration of their shapes. 2D and 3D image processing operations were carried out using the open source software ImageJ (Schneider et al., 2012) and the Skyscan CT-Analyser software (Bruker-microCT N.V., Belgium).

From the binarized datasets of the selected polyhedral inclusions, triangular meshes of their surfaces were then generated using the commercial software VGStudio MAX 2.0 (Volume Graphics GmbH, Germany) that was also employed to visualize 3D renderings of the inclusions. Accurate information about the 3D orientation of the inclusions' facets was extracted using a tool implemented in the free GOM Inspect software (GOM GmbH, Germany). This tool permits a plane to be fitted to a flat surface (e.g. a crystal face) in a 3D mesh by means of a best-fit method, after manually selecting a few points on it. Some poorly developed or irregular facets could not be fitted, hence they were not considered. For each inclusion, the direction of the *xyz* vectors corresponding to the normal to the selected planes were obtained and converted into spherical coordinates, defining for each normal an azimuthal angle (trend) and a polar angle (plunge). These values were then plotted in a stereographic projection (Wulff net, equal-angle projection) using the Stereonet software (Allmendinger et al., 2012; Cardozo and Allmendinger, 2013). The initial orientation of the plane normal vectors in the stereoplot is related to the arbitrary reference system of the 3D dataset. Therefore, the entire set of lines has to be conveniently rotated as a whole, in a few steps around different axes, in order to match (with a tolerance usually lower than 2°) the theoretical position of symmetry elements in garnet (m3m point group). The operation was straightforward when the presence of three- or four-fold axes was evident in the 3D model of the inclusion but this was not always the case, especially for the smallest and less regular inclusions. For all investigated inclusions, the symmetric arrangement of the normal to the crystal facets in the stereoplot was found to be in excellent agreement with a combination of rhombic dodecahedron (12

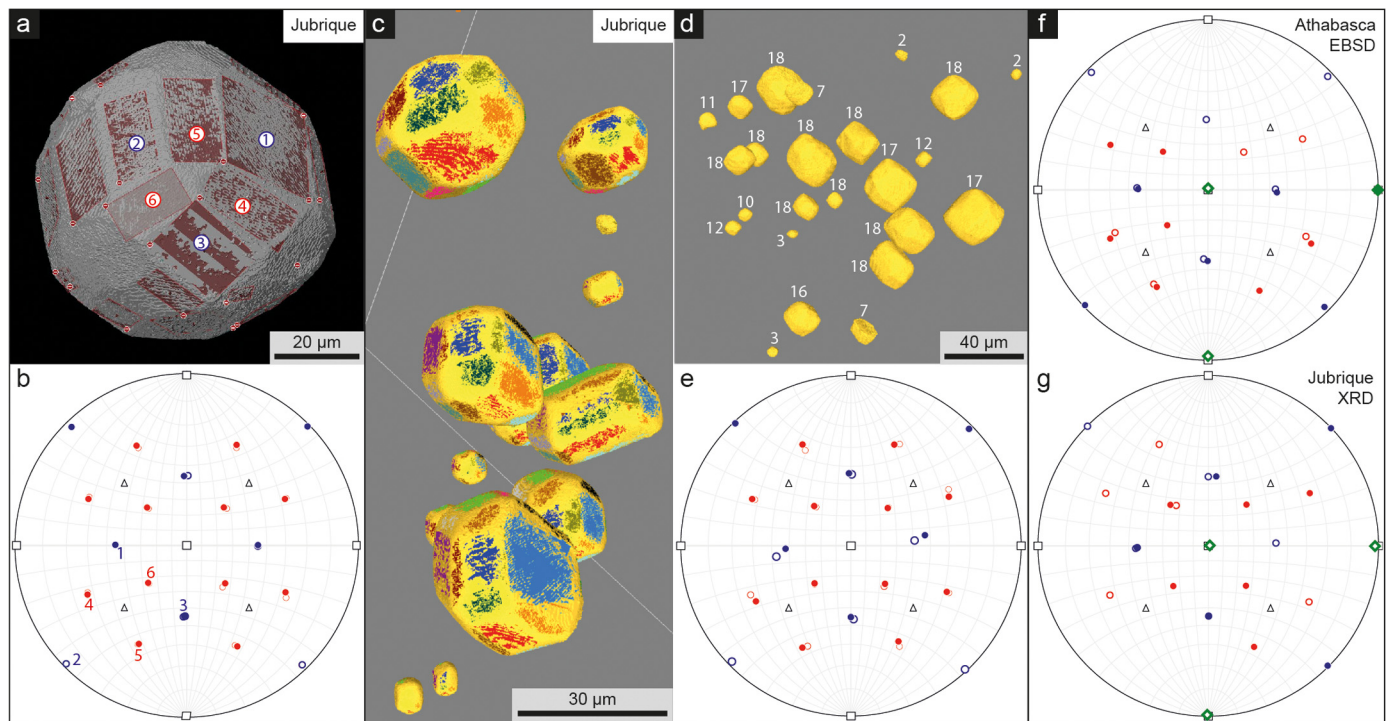


Fig. 2. Shape of quartz inclusions and crystallographic orientation of garnet in granulite-facies samples. **a**, 3D rendering of a single inclusion with shading and numbering highlighting the planes fitted by means of a semi-automatic procedure of face recognition. **b**, stereoplot of the poles of the facets identified for the inclusion in **a**. Wulff net projection highlights coherence of facet orientations with the forms of dodecahedron (blue poles) and icositetrahedron (red poles). Numbers identify the reference facets labeled in **a**. Filled symbols: upper hemisphere poles; empty symbols: lower hemisphere poles. Empty black triangles and squares: ideal position of 3- and 4-fold axes in a cubic symmetry. **c**, 3D rendering of a cluster of inclusions with colors identifying facets with equal orientation. **d**, view of the entire cluster detailed in **c**. Numbers indicate how many times the common orientations, out of the 18 possible pairs of faces given by the combination of dodecahedron and icositetrahedron, occur in each inclusion. **e**, stereoplot of the poles of the facets (mean values) identified for the entire cluster of inclusions in **d**. Symbols as in **b**; all samples are from Jubrique (S Spain). **f-g**, Facet orientations of negative crystals with respect to crystallographic axes of the host garnet. Green diamonds: Garnet {001} poles; blue dots: measured poles of facets compatible with dodecahedral planes; red dots: measured poles of facets compatible with icositetrahedral planes. **(f)** inclusion from Athabasca sample, garnet axes determined by EBSD; **(g)** inclusion from Jubrique sample, garnet axes determined by XRD.

facets) and deltoidal icositetrahedron (24 facets), corresponding in the $m\bar{3}m$ point group to the $\{110\}$ and $\{hkk\}$ sets of equivalent planes, respectively (Fig. 2). In order to identify the effective Miller indices of the icositetrahedron, the angles between pairs of normals in a triplet of $\{hkk\}$ planes arranged around a 3-fold axis, e.g. (hkk) , (kjh) and (khk) , were measured in the stereoplots. A very good match was found with the theoretical value of 33.55° , corresponding to the angle between, e.g., the normal to (211) and (121) planes in the $\{211\}$ icositetrahedron, which represents one of the most typical crystallographic features occurring in natural garnets. Small deviations from the expected ideal positions of facets can be attributed to several factors, such as a) real non-perfect planarity of some facets, b) artefacts introduced with the segmentation procedure, and c) irregularities in the meshes generated from the binarized datasets.

The directions of the normals to the two parallel flat surfaces of the sample, i.e. the cut planes of the original section, were also acquired in order to preserve the information about the orientation of each inclusion within the sample reference frame. This step is crucial to compare the morphological symmetry of the inclusions to the crystallographic orientation of the host garnet, determined afterward by means of XRD or EBSD.

In order to assess whether a population of facets compatible with the dodecahedron and icositetrahedron symmetry could be found in an entire cluster of inclusions, we applied the automatic planes recognition tool of the 3D geological interpretation software Virtuoso developed by IFPEN Energies Nouvelles (France), Geosciences Division (https://www.smartanalogue.eu/?page_id=141). This tool allows for the automatic identification of surfaces parallel to a

given surface defined by the operator in a 3D model. A 3D mesh of a cluster of 24 inclusions from the Jubrique samples was analyzed (Fig. 2). A parameter in the recognition process fixes the degree of tolerance in the identification of new planes. This parameter refers to the degree of parallelism between the normal of the input planes and the new identified planes. Tolerance was set to 0.95%, meaning that less than 5% difference between the normal of an input and output plane was required to have a surface on the 3D model attributed to a given family of facets.

2.4. FIB-SEM imaging and EBSD

Some selected quartz inclusions from the Athabasca samples were investigated by slice-and-view serial sectioning using the Advanced Resource Characterisation Facility's Tescan Lyra3 Ga⁺ dual Focused Ion Beam-Scanning Electron Microscope (FIB-SEM) housed in the John de Laeter Centre, Curtin University (Perth, Australia). Before the milling procedure, a 0.3 μm thick layer of platinum was deposited over the pre-selected area to protect the region of interest and limit the curtaining effect caused by ion beam damage. During serial slicing, the Ga⁺ beam was operated at 2 nA and 30 kV accelerating voltage.

EBSD orientation analyses of the host garnets were performed on a Tescan MIRA3 FESEM housed within the John de Laeter Centre at Curtin University, using 70° sample tilt, 20 kV accelerating voltage and ~ 1 nA beam intensity. EBSD data were acquired using an Oxford Instrument Aztec system incorporating a Symmetry EBSD detector and Aztec 4.1 acquisition software. Post-processing analysis of the data was undertaken using the Tango and Mambo

components of Oxford Instruments HKL Channel 5 software (v. 5.12).

An image processing strategy similar to the one adopted for SRXTM data was used to isolate the inclusions from the host garnet in FIB image stacks. Besides the smaller size of the inclusions (ca. 10 μm) compared to those selected from SRXTM data, the main difference here was given by highly anisotropic voxel size of FIB volumetric datasets (25 nm in the imaging plane, 150–200 nm along the slicing direction). This resulted in a step-like appearance of the 3D renderings, and consequently of the mesh surfaces, making the fitting of planes on the inclusions' facets more difficult. The orientations of the crystallographic axes of the garnets hosting the sliced inclusions were determined by means of EBSD analyses and then related to the morphological symmetry shown by the inclusions.

Measurements of crystallographic orientations of quartz inclusions and EBSD mapping was done with a Camscan MX2500 SEM at the Department of Geosciences, University of Padova (Italy), equipped with a NordlysNano EBSD detector and HKL Channel 5 software (v. 5.12).

2.5. X-ray diffraction (XRD)

Crystallographic investigation of the host garnets was performed with a Rigaku-Oxford Diffraction Supernova single-crystal X-ray diffractometer at the Department of Geosciences, University of Padua (Italy), equipped with a high brilliance X-ray micro-source (X-ray radiation wavelength = 0.71073 Å; spot-size at the sample = 0.12 mm) and with a Pilatus 200K detector (Dectris AG, Switzerland). In order to simplify the comparison between morphological orientation of inclusions and crystallographic orientation of the host garnet, SRXTM samples were mounted on the diffractometer without removing each crystal from its glass capillary; the two parallel flat surfaces of the samples were used as a reference for positioning. The OrientXplot software (Angel et al., 2015) was used to treat the orientation matrices of the garnets and determine the directions of the three crystallographic axes (equivalent in the cubic symmetry) relative to a set of reference axes associated with the diffractometer, displaying the result on a stereogram. As the orientation of each studied inclusion relative to the flat surfaces of the samples was previously known from SRXTM volume data, morphological and crystallographic information could be easily related.

3. Results

3.1. 2D and 3D microstructural and crystallographic characterization of quartz inclusions in garnet

In the high- T samples from granulite-facies, garnet grains range from 1 to 10 mm, and quartz inclusions are commonly more abundant, but not exclusively so, in the garnet cores. This zonal distribution is indicative of their entrapment during the growth of the host garnets (Roedder, 1984). Optical petrography revealed that quartz inclusions are faceted and not rounded (Supplementary Fig. S1).

SRXTM on all samples and additional FIB-SEM serial sectioning on two inclusions from the metapelitic granulite-facies Athabasca sample allowed the reconstruction of the 3D distribution, size and shape of quartz inclusions in garnet. Investigated inclusions are commonly 10–100 μm in size, polyhedral, with well-defined facets and edges. The spatial orientation of facets is consistent with 3- and 4-fold symmetry axes (Fig. 1, Supplementary movie S1). In addition, when observing inclusion clusters, the facets display the same orientation for all quartz crystals included in the same garnet grain (Fig. 1e, f, Supplementary movie S2). This observation has a striking similarity to negative crystals observed in fluid and melt inclusions (Roedder, 1984).

Semi-automatic identification of facets applied to a cluster of quartz inclusions (see Materials and Methods), highlights a maximum of 36 common face orientations to be attributed to quartz crystals in the same garnet. Stereographic projections of these facets (Fig. 2) show that the planes are consistent with a cubic symmetry, resulting from the combination of the deltoidal icositetrahedron and rhombic dodecahedron crystal forms (Fig. 1c, d and Fig. 2a–e), i.e., the polyhedra which describe the most common macroscopic habit of garnet. Similarly, biotite inclusions also display polyhedral shapes with cubic symmetry and are morphologically iso-oriented with coexisting quartz (Fig. 3).

The granulite from Swaziland contains numerous examples of “pinch-and-swell-like” pairs or groups of inclusions in contact along small, often cusped necks (Fig. 4 and Supplementary Movie S3). These microstructures, also observed in the other high- T samples (Supplementary Fig. S1d), show strong similarities with geometries developed by the process of “necking down” of fluid inclusions (Roedder, 1984).

Inclusions in the low- T samples are frequently larger in size (up to 150 μm) and are characterized by a very irregular, anhedral shape, locally with a “scalloped” (Dempster et al., 2017)

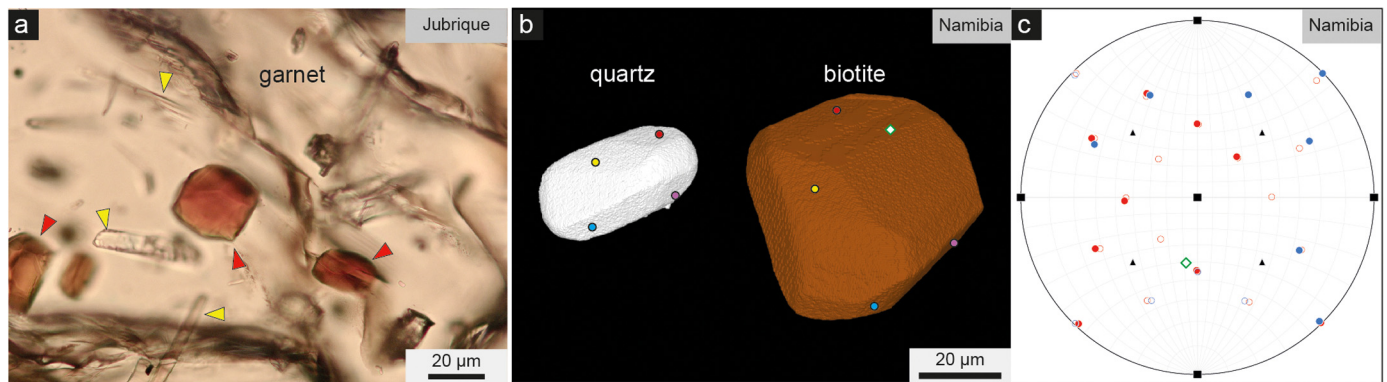


Fig. 3. Evidence of shape maturation in biotite from granulite-facies samples. **a**, inclusions of biotite in garnet (red arrows). The one in the center shows evidence of faceting. Yellow arrows indicate needle-like inclusions of sillimanite. TPLM: transmitted polarized light microscopy. **b**, 3D rendering from SRXTM data of a biotite crystal and an adjacent quartz, both with well-developed crystal faces of parallel orientation. Paired colored dots identify facets with parallel orientation in biotite and quartz, notable in this orientation. **c**, stereonet of the poles of the facets of the crystals visible in **b**, showing coherence with a cubic symmetry for 25 facets of biotite and 11 of quartz. Red: biotite; blue: quartz. Filled circles: upper hemisphere poles; empty circles: lower hemisphere poles. Black squares and triangles: theoretical position of four- and three-fold axes in a model cubic symmetry. Green diamond locates in **b** a facet whose pole in **c** is not compatible with the cubic symmetry of the other facets. Given its large surface it probably corresponds to an original rational plane of biotite.

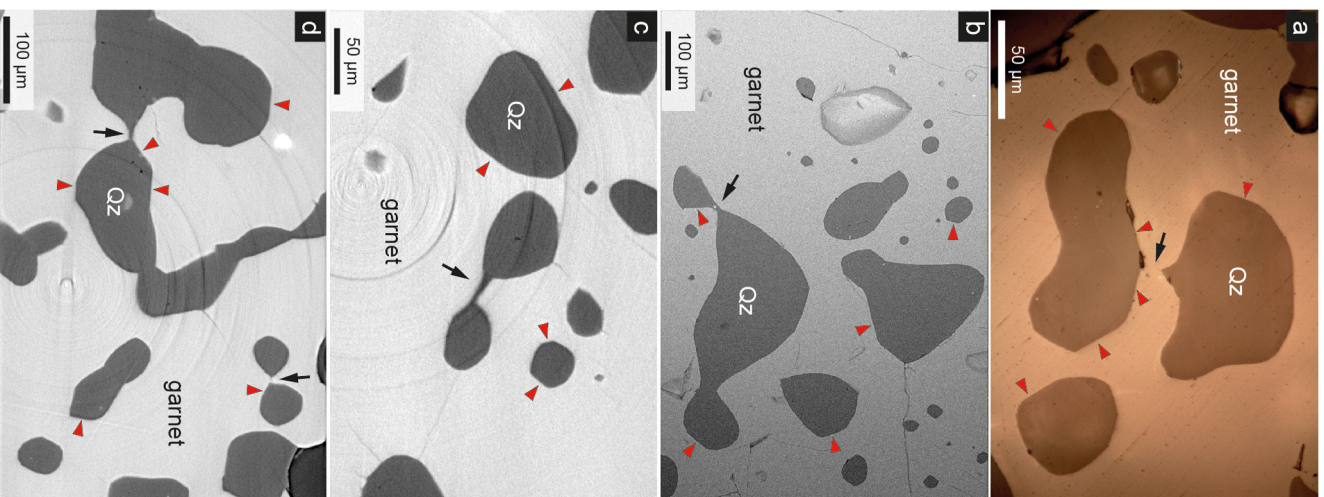


Fig. 4. Evidence of necking down process. All images refer to portions from the granulite-facies sample Swaziland. Black arrows locate the necks; red arrows point to well-developed facets. **a.** BSE-TOPO, backscattered electron microscopy. **b.** BSE-TOPO, backscattered electron microscopy. **c.** PPL, polarized light microscopy. **d.** PPL, polarized light microscopy.

surface (Supplementary Fig. S2 and Movie S4). They are commonly elongate, in places represent clusters of smaller grains, and define an internal foliation. Such irregular shape is commonly observed in quartz from other rocks of the greenschist and lower amphibolite facies ($T < 600^\circ\text{C}$) metamorphic rocks (Spear et al., 2012). The complex shape of these inclusions determines their large surface/volume ratio (S/V) when compared to high- T faceted inclusions having similar volumes (Fig. 5, Table 1). Considering inclusions with a similar volume, e.g., $23 \pm 1 \cdot 10^4 \mu\text{m}^3$, in a low- T sample they have a $S/V = 0.19 \mu\text{m}^{-1}$ whereas in a high- T sample the ratio is $0.09 \mu\text{m}^{-1}$. The latter value indicates a significant surface area reduction, with final values between those of a sphere (the minimum possible) and a cube having equal volume (Fig. 5).

Table 1
Morphometric data of selected inclusions from the studied samples.

Low- T Dataset: Sample	unit	H1-incl 1 east. Alps	H1-incl 2 east. Alps	H1-incl 3 east. Alps	G1-incl 1 Tauern	G1-incl 2 Tauern	G1-incl 3 Tauern	G4-incl 1 Tauern	G4-incl 2 Tauern	G4-incl 3 Tauern	G4-incl 4 Tauern	G4-incl 5 Tauern	G4-incl 6 Tauern	
Inclusion volume	μm^3	86180	73509	72911	243129	173522	161161	86611	50315	40191	11435	8806	7110	
Inclusion surface	μm^2	14292	13365	11950	46654	27936	28273	15566	14232	9399	4505	3846	2706	
Inclusion surface/ volume ratio	μm^{-1}	0.166	0.182	0.164	0.192	0.161	0.175	0.180	0.283	0.234	0.394	0.437	0.381	
Equivalent sphere diameter	μm	54.80	51.97	51.83	77.44	69.20	67.52	54.89	45.80	42.50	27.95	25.62	23.86	
Surface/volume ratio of equivalent volume sphere	μm^{-1}	0.109	0.115	0.116	0.077	0.087	0.089	0.109	0.131	0.141	0.215	0.234	0.251	
High- T Dataset: Sample	unit	X1-incl 1 Jubrique	X1-incl 3 Jubrique	D6-cluster Namibia	A2_i2 Jubrique	A2_i1 Jubrique	F6_i1 Athabasca	F6_i2 Athabasca	D7_i1 Namibia	C1_i1 Massachusetts	F2_i1 Athabasca	F2_i2 Athabasca	F2_i3 Athabasca	F2_i4 Athabasca
Inclusion volume	μm^3	162604	219434	78009	5073	12067	179723	85167	23610	279675	159629	60597	20297	17603
Inclusion surface	μm^2	16680	20250	11000	1703	2880	17894	11242	4936	23993	16669	8560	4075	3790
Inclusion surface/ volume ratio	μm^{-1}	0.103	0.092	0.141	0.336	0.239	0.100	0.132	0.209	0.086	0.104	0.141	0.201	0.215
Equivalent sphere diameter	μm	67.72	74.83	53.01	21.32	28.46	70.02	54.59	35.59	81.14	67.30	48.73	33.84	32.27
Surface/volume ratio of equivalent volume sphere	μm^{-1}	0.089	0.080	0.113	0.281	0.211	0.086	0.110	0.169	0.074	0.089	0.123	0.177	0.186

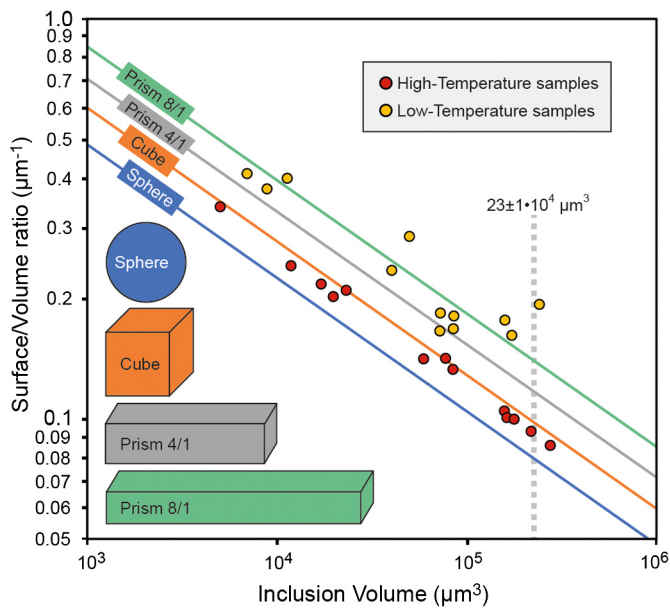


Fig. 5. Morphometric features of low- (greenschist-facies) and high- T (granulite-facies) samples. Log-log diagram of surface/volume ratio (S/V) versus volume of quartz inclusions calculated from SRXTM data. Also reported (colored lines) are the S/V values of a sphere, a cube, and square prisms of 4/1 and 8/1 aspect ratios (sketched on lower left) at given volume. The inclusions from the high- T samples feature small S/V , always lower than volumetric comparable cubes. Conversely, inclusions from low- T samples display very high S/V values, often greater than volumetrically comparable prisms with 8/1 aspect ratio. Vertical dashed line drawn at a volume of $23 \pm 1 \cdot 10^4 \mu\text{m}^3$, as discussed in the text. Data as in Table 1.

SRXTM shows that in general the host-inclusion boundary is generally sharp at the resolution of observation and does not indicate the occurrence of phases other than quartz and garnet along the interface. Rarely, submicrometric, higher density phases (e.g. zircon or rutile) are observed (Fig. 1a, Supplementary Fig. S1g). Less dense phases, suggestive of the presence of fluid in submicrometric pockets at inclusion edges or vertices, have also been observed in some inclusions (Fig. 1a, e, Supplementary Fig. S3). These features are rare in the SRXTM results, and were not observed during FIB-SEM serial sectioning and micro-Raman spectroscopy 3D mapping of inclusions from the Athabasca sample. Combining SRXTM, FIB-SEM and micro-Raman results we can conclude that the occurrence of fluid is more the exception than the rule in the studied high- T quartz inclusions.

3.2. Crystallographic orientation of quartz and garnet

Petrographic analysis of thin sections and quantitative measurement of lattice orientations by EBSD show that the inclusions of quartz in garnet are randomly oriented and show no preferred orientation of their crystallographic axes (a_1 , a_2 , a_3 and c) in a single garnet (Supplementary Fig. S4). In addition, there is no geometric relationship between the main crystallographic axes of quartz inclusions and those of their host garnet.

In contrast, EBSD and single-crystal XRD data demonstrate that the morphological symmetry axes inferred from the orientation of facets within the polyhedral quartz inclusions are systematically parallel to the crystallographic axes of the host garnet (Fig. 2f, g). Such parallelism is expected when polyhedral inclusions form by a process of shape maturation governed by the host phase (Roedder, 1984; Bodnar et al., 1985).

In the cases where adjacent inclusions are connected by thin necks, EBSD data indicate that the single quartz crystals on either side of the neck have different orientation, unrelated to that of the host garnet, and there may be a small crystal with a third

orientation located at the neck of the aggregate (Supplementary Fig. S5). The size and textural position of the small intervening crystal suggests that it has undergone dissolution.

4. Discussion

4.1. Shape maturation process

Strengthened by microstructures indicating the process of “necking down” of polycrystalline quartz inclusions, our observations support the interpretation that shape maturation of quartz inclusions takes place in garnet at high- T (Fig. 6), analogously to the process occurring in fluid and melt inclusions (Bodnar et al., 1985, 1989; Manley, 1996).

The shape of inclusions evolves from irregular to negative crystals to minimize the surface free energy of the host-inclusion system by forming energetically favored facets (Bruno et al., 2014; Einstein, 2015), parallel to rational planes of the host garnet, and by decreasing the inclusion surface/volume and aspect ratios. Although the crystal habit of quartz inclusions might be equivalent to that of garnet, the crystallographic forms defining the inclusions’ faces must obey the trigonal symmetry of quartz (Bruno et al., 2014). Therefore, in the quartz inclusions, each facet must correspond to a rational crystallographic plane of quartz (or a combination of planes), and many will presumably have high indices.

Optical investigation of numerous other granulite samples of worldwide provenance (Supplementary Fig. S6) indicates that the negative crystal shape of quartz inclusions in garnet from high- T rocks is a ubiquitous microstructure that underpins a systematic phenomenon that has been so far overlooked.

Our data indicate that the equilibrium shape is not rounded as previously proposed (Toriumi, 1979; Vernon, 1999; Okamoto and Michibayashi, 2005). Far from being a semantic detail, the very low roundness and high sphericity of the faceted quartz inclusions in high- T samples denotes the novel and fundamental concept that quartz shape is strongly controlled by the host garnet. The polyhedral shape agrees with the Wulff construction (Wulff, 1901) for solids that display (highly) anisotropic surface energies as a function of facet orientation. Although quantitative modeling of the equilibrium shape of quartz inclusions in garnet is hampered by the lack of data on surface energies (Bruno et al., 2014), from a qualitative point of view it can be concluded that in order for garnet to impose that morphology on inclusions, the lowest surface energies among all possible face orientations are those of $\{110\}$ and $\{211\}$ of garnet, respectively the rhombic dodecahedron and the icositetrahedron.

We propose that shape maturation occurs by thermally-activated grain-boundary diffusion along dry interphase boundaries (Joesten, 1991). Little information is available for this process in multiphase aggregates where these boundaries are mobile (Chakraborty, 2008). However, grain boundary diffusion is $>10^4$ times faster than volume diffusion (Chakraborty, 2008), even in the absence of a fluid phase, and the effectiveness of diffusion processes increases by up to 5 orders of magnitude by increasing temperature from 500 to 800 °C (Chakraborty and Ganguly, 1991). Considering available volume diffusion data for garnet (Ganguly et al., 1998), the above constraints imply that interphase boundaries can migrate over distances of 10–100 μm in 1–10 m.y. at high- T (>750 °C, Gualda et al., 2012), but that at low metamorphic temperatures ($<\sim 550$ °C) the process is hindered, and quartz inclusions maintain their irregular shape.

The observations that garnet is able to impose its shape on quartz inclusions but apparently not on sillimanite, and only partially on biotite, recall and confirm the crystalloblastic series of metamorphic minerals. Empirically derived more than one century

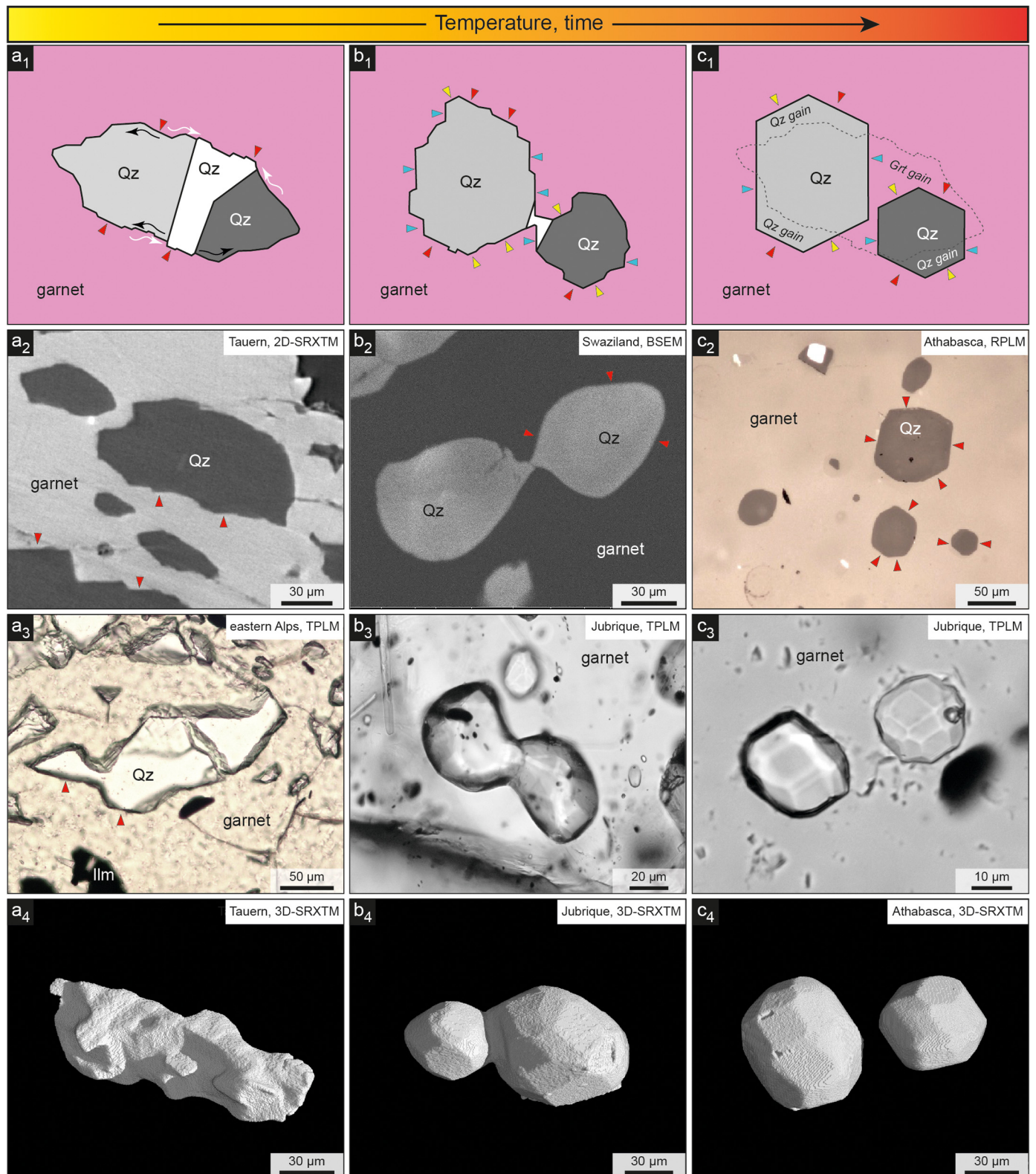


Fig. 6. Model of shape maturation and summary of data. **a₁-c₁**, model of constant-volume (constant-surface in this 2D example) change of shape of an elongated irregular polycrystalline quartz (Qz) inclusion (**a₁**) towards two separate polyhedral inclusions (**c₁**) passing through a stage of “necking down” (**b₁**). During this process the white grain is progressively consumed in favor of the other two gray grains. Colored arrows point to facets parallel to main rational planes of the host garnet (Grt). The dashed line in **a₃** outlines the original Qz shape before modification, constraining areas of net Qz and Grt gain. Black (Si) and white (Al, Fe, Mg, Ca, Mn) arrows schematically illustrate paths of interphase boundary diffusion of elements. **a₂ to a₄**, 2D and 3D views of highly irregular inclusions in low-*T* samples. Red arrows point to parallel rational facets defining a “scaloped” texture. **b₂ to b₄**, 2D and 3D evidence of necking in high-*T* samples. Red arrows point to well-developed facets, particularly prominent in **b₄**. **c₂ to c₄**, 2D and 3D views of negative crystals of quartz in garnet from high-*T* samples. Red arrows as in **b₂**. The polyhedral shape given by the combination of dodecahedron and icositetrahedron is strikingly apparent in the right-side inclusion in **c₃**. On the upper right corner of each panel, sample provenance and visualization technique are reported. 2D = reconstructed axial slice; 3D = volume rendering.

ago (Becke, 1913) and used and taught since, the series lists minerals in order of decreasing tendency to form crystal faces at surfaces of contact with crystals occupying lower positions in the series. The study presented here provides fundamental new data on grain morphology and microstructural evolution in high- T metamorphic rocks. Our approach – the 3D study of inclusions – may serve as a starting point for refining the concept of crystalloblastic series by ordering minerals according to specific (e.g., garnet {211} – quartz) interfacial free energies, as suggested by Kretz (1966), and eventually quantifying absolute values of specific interfacial free energy.

The question of the shape of inclusions, and of its changes with time and temperature, is also of great interest to materials science, for example in the sintering of ceramics (Kingery et al., 1976), with which important comparisons can be made. Firstly, microstructures from materials science help us understand the counterintuitive process of necking down that is observed in some cases in the high- T natural samples (Figs. 4 and 6). In fact, necking down does not lead to the shape with minimum S/V ratio, and to minimization of surface free energy, which would instead be achieved by the opposite process of coarsening by crystal coalescence. However, ceramics can show the same microstructure development through the formation of necks (“de-sintering” process; Lange, 1996) when an inclusion displays a high aspect ratio and mass transfer is achieved by slow diffusion processes such as during solid-solid sintering (Kingery et al., 1976). Thus, the event of necking down is to be expected also in solid inclusions, depending on the interplay between volume and boundary diffusivities, temperature, and the geometrical relations of inclusion/host system. In this respect, the necks observed in this study would represent transitory shapes frozen in the act of developing low S/V forms from high S/V forms. In addition, the maturation of quartz inclusions observed in this study provides new constraints on the behavior of solid-solid systems that can be transferred to the processing of multiphase ceramics. For example, inclusions with negative crystal shape should be expected during the sintering of composites with two phases displaying very different anisotropies in surface energy, thereby affecting the properties of ceramics.

4.2. Implications for thermobarometry and syngensis of inclusions

The overlooked occurrence of shape maturation of quartz inclusions in garnet from high- T metamorphic rocks has twofold important implications for elastic thermobarometry. On one hand, the change to a negative crystal shape adds first-order complexities to the analytical treatment of the mechanics of host-inclusion systems (Mazzucchelli et al., 2018). For example, the sharp edges observed in quartz inclusions represent non-ideal geometries that need to be accounted for in a more accurate analysis. On the other hand, while shape change can reduce the problem of quartz elastic anisotropy (Campomenosi et al., 2018; Bonazzi et al., 2019), by counterbalancing the effects of deviatoric stress and a non-spherical inclusion shape, it will also enhance the effects of viscous relaxation, which are maximized at high- T conditions (Zhong et al., 2020; Moulas et al., 2020). This is the most important consequence for thermobarometry: shape maturation is accompanied by an irreversible strain of the inclusion and host, which is ignored in conventional elastic models and needs to be addressed by a visco-elasto-plastic mechanical model (Zhong et al., 2020). Shape maturation is expected to reset the elastic signal of the internal inclusion pressure at values different from those existing during entrapment. Therefore, the residual pressure recorded applying elastic barometry to inclusions in high- T rocks is not that of entrapment, but reflects the conditions when shape modification was terminated by decreasing temperature (Fig. 7). Depending on the P - T path followed by the rock and the timing of quartz entrapment, under- or overpressures >0.8 GPa can develop in clock-

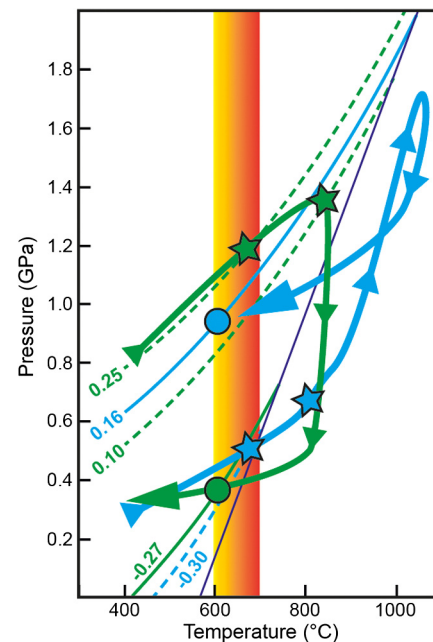


Fig. 7. Effects of shape maturation on recorded residual pressures. Pressure vs. temperature diagram for quartz inclusions in garnet. Thick green and blue lines: P - T paths of studied rocks from Jubrique (Barich et al., 2014) and Athabasca (Dumond et al., 2015), respectively. Stars: conditions of entrapment of quartz inclusions in garnet proposed in the literature. Circles: end of the shape maturation process, assumed to occur when T drops below 600 °C. Vertical yellow-red bar locates the 600-700 °C temperature range. Thin curves are isomekes (lines representing possible entrapment conditions yielding a given residual pressure, P_{inc}) for α quartz – almandine garnet pairs (Angel et al., 2017) labeled with values of P_{inc} (in GPa). Dashed curves: P_{inc} conditions corresponding to entrapment of inclusion; solid curves: P_{inc} conditions after shape maturation and irreversible strain.

wise or anticlockwise trajectories, respectively (Barich et al., 2014; Dumond et al., 2015).

We propose that in nature the shape maturation observed in quartz inclusions in garnet is a general process that may take place in other inclusion-host couples of minerals in which surface energies are significantly lower in the host and where high temperatures, possibly combined with the occurrence of fluids, facilitate grain-boundary diffusion. One possible context are inclusions in diamond. Diamonds are known for their extremely sluggish tracer diffusivity, so low that it would take 10 b.y. for C to diffuse over 10 μm distance at 1200 °C (Koga et al., 2003). This has led to the interpretation that the shape of inclusions in diamonds does not change and can be used to infer relative times of growth of the inclusion with respect to the host diamond. However, as shape change is expected to occur by comparatively more rapid (Joesten, 1991) grain boundary diffusion, it is plausible that small (10-100 μm) inclusions in diamonds could evolve to polyhedral negative crystals over geologically reasonable timeframes of residence at high- T in the mantle. This conclusion is strengthened by the finding of fluid films at diamond/inclusion interfaces (Nimis et al., 2016), that would greatly enhance grain boundary diffusion. Therefore, given the possibility that inclusions in diamond may become polyhedral negative crystals *after* entrapment, the main criterion for the syngensis (co-crystallization) of diamond and their inclusions, i.e., the imposition of the morphology of the host diamond on the inclusion (Meyer, 1987), needs to be critically reconsidered (Taylor et al., 2003).

5. Conclusions

We have showed evidence that mineral inclusions in garnet may undergo post-entrapment shape modifications toward negative crystals in high- T rocks from granulite-facies conditions.

Kretz (1966) had already observed that quartz inclusions in a grain of garnet of a biotite-garnet gneiss from Quebec, Canada, were polyhedral and with commonly oriented facets. He suggested that the garnet imposed the form of the dodecahedron {110} on quartz, but did not speculate further, nor did following researchers, also because of the lack of tools for imaging the much smaller inclusions that we have characterized.

With our study not only we show that the forgotten intuitions of Kretz (1966) were correct, but also that the polyhedral shape is acquired after entrapment, and that garnet imposes on quartz, but also in part on biotite, a combination of the {110} and {211} forms. We also show that such shape maturation is ubiquitous in rocks from high-grade metamorphic terranes worldwide.

These results need to be accounted for when applying elastic barometry to rocks which have spent part of their P - T - t path at $T > 700$ °C, and when considering the shape of an inclusion as indicative of its relative age of formation with respect to its host. They also represent a new bridge joining geosciences with ceramics and metallurgy when dealing with microstructure development.

CRediT authorship contribution statement

B.C. developed the concept, collected the bulk of the samples and carried out the petrographic and microstructural study. M.P., L.M. and F.M. performed the SRXTM experiments and M.P. and M.F. the analysis of SRXTM data. L.P. and R.S. performed the SEM and EBSD analyses, respectively. T.T. and S.R. performed the FIB-SEM analyses. F.N. performed the XRD analyses. B.C. wrote the paper. All authors were involved in multiple revisions of the text and figures.

Declaration of competing interest

The authors declare that they have no known competing financial interests or personal relationships that could have appeared to influence the work reported in this paper.

Acknowledgements

S. Ferrero prompted this research with a sentence in a manuscript. We wish to thank S. Carmignato and F. Zanini for suggestions on tomographic data analysis methods; S. Ferrero and M.A. Ziemann for help with micro-Raman analysis; A. Bonnin for technical assistance with SRXTM analysis; D. Fougereuse and W. Rickard for technical suggestions during FIB-SEM analyses; IFPEN Energies Nouvelles for allowing use of the Virtuoso software; G. Dumond, J. Taylor and J.A. Thomson for providing samples. The manuscript benefited from reviews by D. Pattison and an anonymous reviewer. Discussions with B. Bodnar, M. Holness, L.S. Hollister and P. Nimis and critical reading of the manuscript draft by J.A.D. Connolly are also gratefully acknowledged. The Paul Scherrer Institut, Villigen (Switzerland) granted synchrotron radiation beamtime at the TOM-CAT beamline X02DA of the SLS (exp. 20181644).

Funding: B.C. acknowledges financial support from University of Padova (grant BIRD183984) and MIUR (grant 2017ZE49E7).

Appendix A. Supplementary material

Supplementary material related to this article can be found online at <https://doi.org/10.1016/j.epsl.2020.116708>.

References

Allmendinger, R.W., Cardozo, N., Fisher, D.M., 2012. Structural Geology Algorithms: Vectors and Tensors in Structural Geology. Cambridge Univ. Press, Cambridge.

- Angel, R.J., Mazzucchelli, M.L., Alvaro, M., Nimis, P., Nestola, F., 2014. Geobarometry from host inclusion systems: the role of elastic relaxation. *Am. Mineral.* 99, 2146–2149.
- Angel, R.J., Milani, S., Alvaro, M., Nestola, F., 2015. OrientXplot: a program to process and display relative crystal orientations. *J. Appl. Crystallogr.* 48, 1330–1334.
- Angel, R.J., Mazzucchelli, M.L., Alvaro, M., Nestola, F., 2017. EosFit-Pinc: a simple GUI for host-inclusion elastic thermobarometry. *Am. Mineral.* 102, 1957–1960.
- Barich, A., Acosta-Vigil, A., Garrido, C.J., Cesare, B., Tajčmanová, L., Bartoli, O., 2014. Microstructures and petrology of melt inclusions in the anatectic sequence of Jubrique (Betic Cordillera, S Spain): implications for crustal anatexis. *Lithos* 206–207, 303–320.
- Baruchel, J., Cloetens, P., Härtwig, J., Ludwig, W., Mancini, L., Pernot, P., Schlenker, M., 2000. Phase imaging using highly coherent X-rays: radiography, tomography, diffraction topography. *J. Synchrotron Radiat.* 7, 196–201.
- Becke, F., 1913. Über Mineralbestand und Struktur der krystallinen Schiefer. *Denkschriften der Akademie der Wissenschaften. Math. Naturwiss. Kl* 75, 1–53.
- Blamey, N.J.F., Parnell, J., McMahon, S., Mark, D.F., Tomkinson, T., Lee, M., Shivak, J., Izawa, M.R.M., Banerjee, N.R., Flemming, R.L., 2015. Evidence for methane in Martian meteorites. *Nat. Commun.* 6, 7399.
- Bodnar, R.J., Reynolds, T.J., Kuehn, C.A., 1985. Fluid inclusion systematics in epithermal systems. *Rev. Econ. Geol.* 2, 73–98.
- Bodnar, R.J., Binns, P.R., Hall, D.L., 1989. Synthetic fluid inclusions - VI. Quantitative evaluation of the decrepitation behaviour of fluid inclusions in quartz at one atmosphere confining pressure. *J. Metamorph. Geol.* 7, 229–242.
- Bonazzi, M., Tumiati, S., Thomas, J.B., Angel, R.J., Alvaro, M., 2019. Assessment of the reliability of elastic geobarometry with quartz inclusions. *Lithos* 350–351, 105201.
- Bruno, M., Massaro, F.R., Principe, M., Demichelis, R., De La Pierre, M., Nestola, F., 2014. Ab initio calculations of the main crystal surfaces of forsterite (Mg₂SiO₄): a preliminary study to understand the nature of geochemical processes at the olivine interface. *J. Phys. Chem. C* 118, 2498–2506.
- Campomenosi, N., Mazzucchelli, M.L., Mihailova, B.D., Scambelluri, M., Angel, R.J., Nestola, F., Reali, A., Alvaro, M., 2018. How geometry and anisotropy affect residual strain in host-inclusion systems: coupling experimental and numerical approaches. *Am. Mineral.* 103, 2032–2035.
- Cardozo, N., Allmendinger, R.W., 2013. Spherical projections with OSXstereonet. *Comput. Geosci.* 51, 193–205.
- Cesare, B., Nestola, F., Johnson, T., Mugnaioli, E., Della Ventura, G., Peruzzo, L., Bartoli, O., Viti, C., Erickson, T., 2019. Garnet, the archetypal cubic mineral, grows tetragonal. *Sci. Rep.* 9, 14672.
- Chakraborty, S., 2008. Diffusion in solid silicates: a tool to track timescales of processes comes of age. *Annu. Rev. Earth Planet. Sci.* 36, 153–190.
- Chakraborty, S., Ganguly, J., 1991. Compositional zoning and cation diffusion in aluminosilicate garnets. In: Ganguly, J. (Ed.), *Diffusion, Atomic Ordering, and Mass Transport*. In: *Adv. Phys. Geochem.*, vol. 8. Springer, New York, pp. 120–175.
- Chopin, C., 1984. Coesite and pure pyrope in high-grade blueschists of the Western Alps: a first record and some consequences. *Contrib. Mineral. Petrol.* 86, 107–118.
- Dempster, T.J., La Piazza, J., Taylor, A.G., Beaudoin, N., Chung, P., 2017. Chemical and textural equilibration of garnet during amphibolite facies metamorphism: the influence of coupled dissolution–reprecipitation. *J. Metamorph. Geol.* 35, 1111–1130.
- Diener, J.F.A., White, R.W., Link, K., Dreyer, T.S., Moodley, A., 2013. Clockwise, low- P metamorphism of the Aus granulite terrain, southern Namibia, during the Mesoproterozoic Namaqua Orogeny. *Precambrian Res.* 224, 629–652.
- Dumond, G., Goncalves, P., Williams, M.L., Jercinovic, M.J., 2015. Monazite as a monitor of melting, garnet growth and feldspar recrystallization in continental lower crust. *J. Metamorph. Geol.* 33, 735–762.
- Einstein, T.L., 2015. Equilibrium shape of crystals. In: Nishinaga, T. (Ed.), *Handbook of Crystal Growth, Fundamentals*, 2nd ed. Elsevier, Amsterdam, pp. 215–264.
- Ferrero, S., Angel, R.J., 2018. Micropetrology: are inclusions grains of truth? *J. Petrol.* 59, 1671–1700.
- Ganguly, J., Cheng, W., Chakraborty, S., 1998. Cation diffusion in aluminosilicate garnets: experimental determination in pyrope–almandine diffusion couples. *Contrib. Mineral. Petrol.* 131, 171–180.
- Gualda, G.A.R., Pamukcu, A.S., Ghiorsio, M.S., Anderson Jr, A.T., Sutton, S.R., Rivers, M.L., 2012. Timescales of quartz crystallization and the longevity of the Bishop giant magma body. *PLoS ONE* 7, e37492.
- Harris, J.W., 1968. The recognition of diamond inclusions. Part 1: syngenetic inclusions. *Ind. Diamond Rev.* 28, 402–410.
- Hopkins, M., Harrison, M.T., Manning, C.E., 2008. Low heat flow inferred from >4 Gyr zircons suggests Hadean plate boundary interactions. *Nature* 456, 493–496.
- Joesten, R., 1991. Grain-boundary diffusion kinetics in silicate and oxide minerals. In: Ganguly, J. (Ed.), *Diffusion, Atomic Ordering, and Mass Transport*. In: *Advances in Physical Geochemistry*, vol. 8. Springer, New York, pp. 345–395.
- Kingery, W.D., Bowen, H.K., Uhlmann, D.R., 1976. *Introduction to Ceramics*. Wiley, 1056 pp.
- Koga, K.T., Van Orman, J.A., Walter, M.J., 2003. Diffusive relaxation of carbon and nitrogen isotope heterogeneity in diamond: a new thermochronometer. *Phys. Earth Planet. Inter.* 139, 35–43.

- Kohn, M., 2014. "Thermoba-Raman-try": calibration of spectroscopic barometers and thermometers for mineral inclusions. *Earth Planet. Sci. Lett.* 388, 187–196.
- Kretz, R., 1966. Interpretation of the shape of mineral grains in metamorphic rocks. *J. Petrol.* 7, 68–94.
- Lange, F.F., 1996. De-sintering, a phenomena concurrent with densification within powder compacts: a review. In: German, R.M., Messing, G.L., Cornwal, R.G. (Eds.), *Sintering Technology*. Marcel Dekker Pubs, New York, pp. 1–12.
- Liu, J., Xia, Q.-K., Kuritani, T., Hanski, E., Yu, H.-R., 2017. Mantle hydration and the role of water in the generation of large igneous provinces. *Nat. Commun.* 8, 1824.
- Manley, R., 1996. Morphology and maturation of melt inclusions in quartz phenocrysts from the Badlands rhyolite lava flow, southwestern Idaho. *Am. Mineral.* 81, 158–168.
- Marone, F., Stampanoni, M., 2012. Regridding reconstruction algorithm for real time tomographic imaging. *J. Synchrotron Radiat.* 19, 1029–1037.
- Mazzucchelli, M.L., Burnley, P., Angel, R.J., Morganti, S., Domeneghetti, M.C., Nestola, F., Alvaro, M., 2018. Elastic geothermobarometry: corrections for the geometry of the host-inclusion system. *Geology* 46, 231–234.
- Meyer, H.O.A., 1987. Inclusions in diamonds. In: Nixon, P.H. (Ed.), *Mantle Xenoliths*. John Wiley & Sons, Chichester, U.K., pp. 501–522.
- Moulas, E., Kostopoulos, D., Podladchikov, Y., Chatzitheodoridis, E., Schenker, F.L., Zingerman, K.M., Pomonis, P., Tajčmanová, L., 2020. Calculating pressure with elastic geobarometry: a comparison of different elastic solutions with application to a calc-silicate gneiss from the Rhodope Metamorphic Province. *Lithos* 378–379, 105803.
- Nabiei, F., Badro, J., Dennenwaldt, T., Oveisi, E., Cantoni, M., Hébert, C., El Goresy, A., Barrat, J.-A., Gillet, P., 2018. A large planetary body inferred from diamond inclusions in a ureilite meteorite. *Nat. Commun.* 9, 1327.
- Nestola, F., Korolev, F.N., Kopylova, M., Rotiroti, N., Pearson, D.G., Pamato, M.G., Alvaro, M., Peruzzo, L., Gurney, J.J., Moore, A.E., Davidson, J., 2018. CaSiO₃ perovskite in diamond indicates the recycling of oceanic crust into the lower mantle. *Nature* 555, 237–241.
- Nimis, P., Alvaro, M., Nestola, F., Angel, R.J., Marquardt, K., Rustioni, G., Harris, J.W., Marone, F., 2016. First evidence of hydrous silicic fluid films around solid inclusions in gem-quality diamonds. *Lithos* 260, 384–389.
- Okamoto, A., Michibayashi, K., 2005. Progressive shape evolution of a mineral inclusion under differential stress at high temperature: example of garnet inclusions within a granulite-facies quartzite from the Lützow-Holm Complex, East Antarctica. *J. Geophys. Res.* 110, B11203.
- Paganin, D., Mayo, S.C., Gureyev, T.E., Miller, P.R., Wilkins, S.W., 2002. Simultaneous phase and amplitude extraction from a single defocused image of a homogeneous object. *J. Microsc.* 206, 33–40.
- Richardson, S.H., Gurney, J.J., Erlank, A.J., Harris, J.W., 1984. Origin of diamonds in old enriched mantle. *Nature* 310, 198–202.
- Roedder, E., 1984. Fluid Inclusions. *Rev. Mineralogy*, vol. 12. Min. Soc. America.
- Rubatto, D., Regis, D., Hermann, J., Boston, K., Engi, M., Beltrando, M., McAlpine, S.R.B., 2011. Yo-Yo subduction recorded by accessory minerals in Italian Western Alps. *Nat. Geosci.* 4, 338–342.
- Schneider, C.A., Rasband, W.S., Eliceiri, K.W., 2012. NIH image to ImageJ: 25 years of image analysis. *Nat. Methods* 9, 671–675.
- Silverstone, J., Munoz, J.L., 1987. Fluid heterogeneities and hornblende stability in interlayered graphitic and nongraphic schists (Tauern Window, Eastern Alps). *Contrib. Mineral. Petrol.* 96, 426–440.
- Spear, F.S., Ashley, K.T., Webb, L.E., Thomas, J.B., 2012. Ti diffusion in quartz inclusions: implications for metamorphic time scales. *Contrib. Mineral. Petrol.* 164, 977–986.
- Spear, F.S., Thomas, J.B., Hallett, B.W., 2014. Overstepping the garnet isograd: a comparison of QuiG barometry and thermodynamic modeling. *Contrib. Mineral. Petrol.* 86, 1059.
- St-Onge, M.R., 1987. Zoned poikiloblastic garnets: P-T paths and syn-metamorphic uplift through 30 km of structural depth, Wopmay Orogen. *Can. J. Petrol.* 28, 1–22.
- Stampanoni, M., Groso, A., Isenegger, A., Mikuljan, G., Chen, Q., Bertrand, A., Henein, S., Betemps, R., Frommherz, U., Böhrer, P., Meister, D., Lange, M., Abela, R., 2006. Trends in synchrotron-based tomographic imaging: the SLS experience. *Developments in X-ray tomography V. Proc. SPIE* 6318, U199–U212.
- Tacchetto, T., Bartoli, O., Cesare, B., Berkesi, M., Aradi, L.E., Dumond, G., Szabó, C., 2019. Multiphase inclusions in peritectic garnet from granulites of the Athabasca granulite terrane (Canada): evidence of carbon recycling during Neoproterozoic crustal melting. *Chem. Geol.* 508, 197–209.
- Taylor, J., Stevens, G., Armstrong, R., Kisters, A.F.M., 2010. Granulite facies anatexis in the Ancient Gneiss Complex, Swaziland, at 2.73 Ga: mid-crustal metamorphic evidence for mantle heating of the Kaapvaal craton during Ventersdorp magmatism. *Precambrian Res.* 177, 88–102.
- Taylor, L.A., Anand, M., Promprated, P., 2003. Diamonds and their inclusions: are the criteria for syngeneis valid?. In: *Proc. 8th Int. Kimberlite Conf.*, vol. 1, pp. 1–5.
- Thomson, J.A., 2001. A counterclockwise P-T path for anatectic pelites, south-central Massachusetts. *Contrib. Mineral. Petrol.* 141, 623–641.
- Toriumi, M.A., 1979. Mechanism of shape-transformation of quartz inclusions in albite of regional metamorphic rocks. *Lithos* 12, 325–333.
- Vernon, R.H., 1999. Quartz and feldspar microstructures in metamorphic rocks. *Can. Mineral.* 37, 513–524.
- Vernon, R.H., 2004. *A Practical Guide to Rock Microstructure*. Cambridge Univ. Press, Cambridge.
- Walter, M.J., Kohn, S.C., Araujo, D., Bulanova, G.P., Smith, C.B., Gaillou, E., Wang, J., Steele, A., Shirey, S.B., 2011. Deep mantle cycling of oceanic crust: evidence from diamonds and their mineral inclusions. *Science* 334, 54–57.
- Wilde, S.A., Valley, J.W., Peck, W.H., Graham, C.M., 2001. Evidence from detrital zircons for the existence of continental crust and oceans on the Earth 4.4 Gyr ago. *Nature* 409, 175–178.
- Wulff, G., 1901. Zur Frage der Geschwindigkeit des Wachstums und der Auflösung der Kristallflächen. *Z. Kristallogr. Kristallgeom.* 34, 449–530.
- Zack, T., Moraes, R., Kronz, A., 2004. Temperature dependence of Zr in rutile: empirical calibration of a rutile thermometer. *Contrib. Mineral. Petrol.* 148, 471–488.
- Zhong, X., Moulas, E., Tajčmanová, L., 2020. Post-entrapment modification of residual inclusion pressure and its implications for Raman elastic thermobarometry. *Solid Earth* 11, 223–240.